Kinetic modelling of runaway electrons and their mitigation in ITER

P. Aleynikov[1], K. Aleynikova[2], B. Breizman[3], G. Huijsmans[1], S. Konovalov[2], S. Putvinski[4], V. Zhogolev[2]

[1]ITER Organization, Route de Vinon-sur-Verdon, CS 90 046, 13067 St. Paul Lez Durance Cedex, France
[2]NRC Kurchatov Institute, Kurchatov sq. 1, Moscow, 123098 Russia
[3]Institute for Fusion Studies, The University of Texas, Austin, Texas, 78712 USA
[4]Tri Alpha Energy, Inc., P.O.Box 7010, Rancho Santa Margarita, CA, 92688-7010 USA

pavel.aleynikov@iter.org

1. Introduction

Runaway electrons (RE) can be generated during plasma disruptions in ITER. A large portion of the toroidal current can then be carried by RE, so that a substantial fraction of the magnetic energy would be associated with the RE current. The uncontrolled loss of such REs in ITER must be avoided to minimize the detrimental effects of disruptions. It is therefore crucial to understand the processes leading to the generation and loss of RE beams, and to develop adequate means to control or suppress the RE beams in ITER. This paper presents simulations of RE generation during ITER disruptions and assessment of RE suppression mechanisms.

Massive Gas Injection (MGI) has been used successfully to mitigate disruptions in present tokamaks, and is therefore considered to be an essential component of the envisioned ITER Disruption Mitigation System (DMS). The target electron density $n_R = 4.0 \cdot 10^{22} m^{-3}$ [1] required to suppress RE in ITER reliably is known to be beyond ITER technical limits. However, it has been shown in recent DIII-D experiments, that MGI of high-Z impurities (Ar,Ne,...) causes a fast current decay of the RE current at much lower densities than expected [2]. The reported decay time is significantly shorter than the slowing down time of the RE beam on plasma electrons (the time that determines the RE avalanche threshold [3]). This surprisingly high efficiency of MGI in DIII-D can be explained by the scattering of REs on screened high-Z nuclei [4], which facilitates the suppression of the RE current.

There are also experimental indications [5] that the threshold E-field for RE onset may be several times higher than the critical field $E_c = \frac{4\pi e^3 n_e ln\Lambda}{mc^2}$ needed to overcome the electron drag. These findings call for refined theoretical assessment of RE generation and mitigation.

In the present work, we calculate the ITER MGI target parameters taking into account effect of high-Z nuclei. We solve a 2D Fokker-Planck equation for REs (with a refined secondary electron source and with self-consistent calculation of the driving electric field). To describe the high-Z impurity content we have developed 1D transport code which calculates self-consistent radial profiles of the bulk plasma parameters and impurities.

2. Kinetic equation

Following [3, 6] we solve a 2D bounce averaged Fokker-Planck equation:

$$\frac{\partial f}{\partial t} = \langle L_E (f_{re}) \rangle + \langle C (f_{re}) \rangle + \langle L_{rad} (f_{re}) \rangle + \langle S \rangle, \tag{1}$$

where operators in the right-hand side represent: $\langle L_E (f_{re}) \rangle$ - electric field, $\langle C (f_{re}) \rangle$ - Coulomb collisions, $\langle L_{rad} (f_{re}) \rangle$ - radiation losses (both synchrotron and bremsstrahlung) and $\langle S \rangle$ represents knock-on collisions source. The equation is solved using Monte Carlo method. The bounce averaging is done analytically in terms of elliptic integrals. The Langevin equivalent operators are taken from [3, 6].

2.1. Collisional friction force

In cold plasmas with impurities, bound electrons as well as free electrons contribute to the friction force for the runaways. To capture this effect an effective electron density $n_e^{eff} = n_e^{free} + 0.5 n_e^{bound}$ is introduced in [3] in the collision operator.

To calculate the friction force more accurately, we follow [7] and use Bethe's stopping power formula with an effective ion potential E_{eff} determined by the Thomas-Fermi model. Then the stopping power for a relativistic electron becomes

$$Q_{loss} = \frac{4\pi e^4}{m_Z m_e c^2} \frac{\gamma^2}{\gamma^2 - 1} (Z_0 - Z) \left\{ \ln \left(\frac{m_e c^2}{E_{eff}} \right) + \ln \left(\frac{\gamma^2 - 1}{\sqrt{\gamma + 1}} \right) \right\}, \tag{2}$$

where m_e and m_Z are the electron rest mass and atomic mass of impurity respectively, γ is the relativistic factor of an electron, Z and Z_0 are an ion charge and a full nuclei charge respectively and E_{eff} is calculated according to equation (51) in [7].

Figure 1 shows the stopping power in a plasma with $10^{20} m^{-3}$ Hydrogen and $0.2 \cdot 10^{20} m^{-3}$ Argon at $1.5 eV$. We note that the stopping power given by (2) (red dotted curve) agrees well with the ESTAR [8] (blue curve). And while the "$0.5 n_e^{bound}$" approximation (green curve) is reasonably accurate within the energy range $0.1 - 1 MeV$ it clearly overestimates the friction for lower energy runaways and underestimates it for higher energies. Stopping power on free electrons is indicated by red dashed curve.
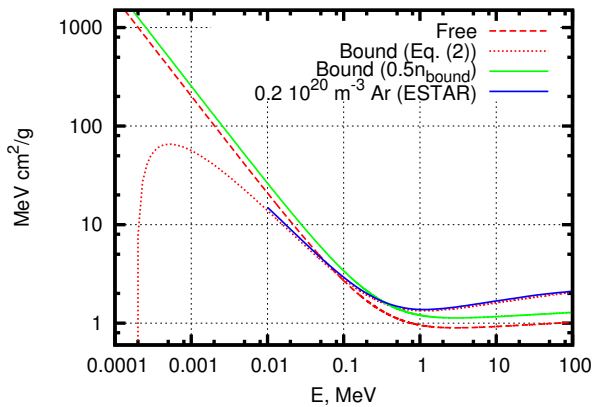

Figure 1. Collisional stopping power in plasma with $10^{20} m^{-3}$ H and $0.2 \cdot 10^{20} m^{-3}$ Ar at $1.5 eV$
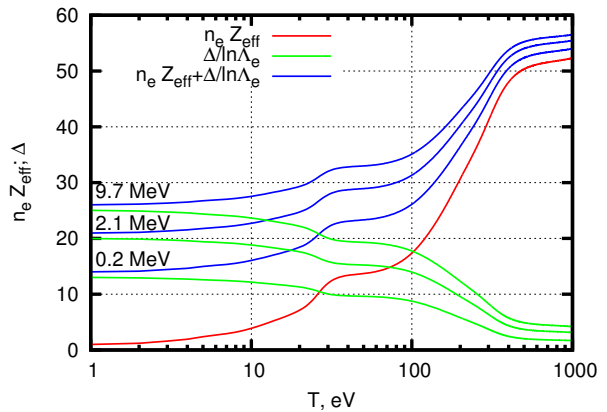
Figure 2. Temperature dependence of scattering for plasma with $0.2 \cdot 10^{20} m^{-3} Ar.$

2.2. Elastic scattering

As it was shown in [4], scattering of high energy runaways on high-Z nuclei plays a major role in runaways dynamics. Formally, the fast electron scattering on high-Z impurity nuclei in the pitch angle scattering operator [3, 6] is accounted for by substitution

$$Z_{eff} \equiv \frac{1}{n_e} \sum_Z \sum_{k=0}^Z n_Z^k k^2 \Rightarrow \frac{1}{n_e \ln \Lambda} \sum_Z \sum_{k=0}^Z n_Z^k \{k^2 \ln \Lambda + \Delta_k\}, \tag{3}$$

where n_Z^k is the density of ions in charge state k, and Δ_k (defined in [4, 7]) takes into account interaction of runaways with screened ions nuclei charge according to Thomas-Fermi model.

Figure 2 shows contributions from both terms in (3) to the total scattering effect for runaways with different energies in plasma with $10^{20} m^{-3}$ of Hydrogen and $0.2 \cdot 10^{20} m^{-3}$ of Argon. The red curve represents Coulomb scattering on ions with Z_{eff} charges depending on plasma temperature. It grows with temperature due to the ionization of Argon. Green curves represents "unaccounted" scattering effect Δ due to interaction of high energy electron with Ar nuclei. At high temperate Ar atoms are fully ionized and Δ vanishes. An immediate conclusion that follows form figure 2 is that at low temperature plasmas ($< 20eV$) with significant high-Z impurities content the scattering of runaways is strongly enhanced by interaction with impurity nuclei.

2.3. Synchrotron radiation

Although synchrotron radiation does not affect the low-energy part of the RE spectra, it plays an important role by providing an additional energy loss mechanism and limiting the maximum energy of runaways. Indeed, as it was shown in [9], RE energy gain in presence of synchrotron loss is expressed

$$\frac{d\gamma}{dt} = \frac{e(E - E_c)}{m_e c} - \frac{1}{\tau_{rad}} \theta^2 \gamma^2, \tag{4}$$

where θ is an electron pitch-angle, $\tau_{rad}[s] = \frac{3m^3 c^5}{2e^4 B^2} = \frac{5}{B^2[Tesla]}$ is a synchrotron radiation time constant. Pitch-angle scattering

$$\frac{d}{dt} \left(\gamma^2 \theta^2 \right) = \frac{Z}{\tau}. \tag{5}$$

where $\tau = \frac{m_e c}{e E_c}$ is a collisional time constant. Combination of (4) and (5) reveals that energy growth is limited by synchrotron losses:

$$\gamma = \gamma_0 + \frac{e(E - E_c)}{mc} t - \frac{t^2}{2} \frac{Z}{\tau \tau_{rad}}; \tag{6}$$

$$\gamma_{max} = \frac{\tau_{rad}}{2Z\tau} \left(\frac{E}{E_c} - 1 \right)^2. \tag{7}$$

The analytical estimate of the cut-off energy (7) agrees very well with the numerical calculations. On the figure 3 normalized RE spectra are shown. Blue curves represent quasi-stationary solution at constant electric field $E = 5E_c$, Hydrogen density $n_H = 10^{20} m^{-3}$ and different Argon densities. The resulting average energy is 5.6, 7.5 and $9.1 MeV$ in case Argon density is 0.5, 0.25 and $0.1 \cdot 10^{20} m^{-3}$ respectively. For ITER $\frac{\tau_{rad}}{2\tau} \approx 10$.

With synchrotron radiation switched off no quasi-stationary solution can be obtained and at constant electric field energy grows continuously.
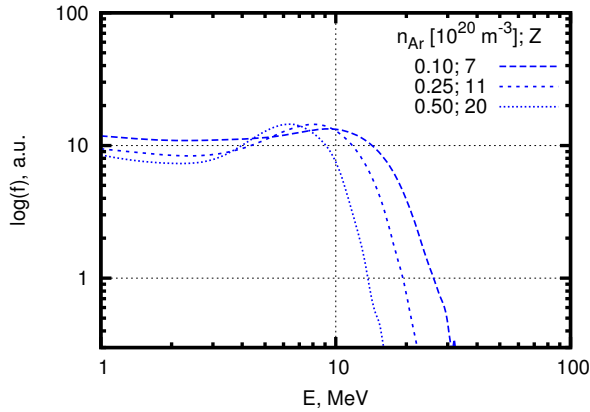
Figure 3.   Normalized quasi-stationary RE spectra at constant $E = 5E_c$ for different Argon impurity densities. Hydrogen density $10^{20}m^{-3}$, Argon densities are 0.5, 0.25 and $0.1 \cdot 10^{20}m^{-3}$.
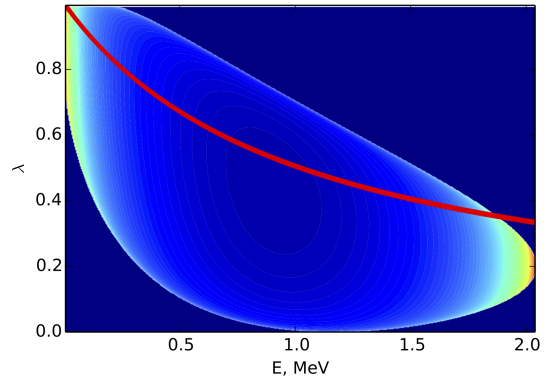
Figure 4. The knock-on collisions source terms. Red curve - shape of the simplified source [3]; Color-coded - a secondary electrons source (8) for primary electron with $\gamma_0 \approx 5$ and $\lambda_0 = 0.2$

2.4. Knock-on collisions

The avalanche is the dominant mechanism of RE generation in ITER. In [3] (and later in [6]) a simplified model for knock-on source operator was used. Simplified operator implied an ultra-relativistic primary electron with $\gamma_0 >> 1$ and $\theta_0 = 0$. These constraints need to be relaxed for three reasons: a) enhanced scattering on high-Z impurities may prohibit high anisotropy of the beam; b) at low electric field RE energy is limited by synchrotron radiation according to (7); c) at very high electric field ($E > 100E_c$) the moderate energy electrons (keV range) are involved in the avalanche process, the collisionality for such electrons is much higher than for ultra-relativistic electrons, thus it is important to calculate knock-on collisions for such electrons accurately.

In our calculations we use full non-simplified source operator

$$S = n_{full}c\frac{\sqrt{\gamma_0^2 - 1}}{\gamma_0}\left\langle \delta\left[\cos\theta - \cos\theta_p\right]\right\rangle\frac{d\sigma}{d\Delta}, \qquad (8)$$

where n_{full} is a total electron density of free and bound electrons (due to the fact that kinetic energy of RE are higher the ionization energy for impurities and in case of close collision bound electron will be knocked from it's orbit) and the differential cross-section $\frac{d\sigma}{d\Delta}$ is defined by Møller scattering formula

$$\frac{d\sigma}{d\Delta} = \frac{2\pi r_e^2}{\gamma_0^2 - 1}\left\{\frac{(\gamma_0 - 1)^2\gamma_0^2}{(\gamma - 1)^2(\gamma_0 - \gamma)^2} - \frac{2\gamma_0^2 + 2\gamma_0 - 1}{(\gamma - 1)(\gamma_0 - \gamma)} + 1\right\}, \qquad (9)$$

where r_e is the classical electron radius and γ is a relativistic factor of the secondary electron. The gyro-averaged δ-function in (8) is

$$\left\langle \delta\left[\cos\theta - \cos\theta_p\right]\right\rangle = \frac{1}{\pi}\frac{1}{\sqrt{\left(\frac{p_\perp p_{0\perp}}{pp_0}\right)^2 - \left(\frac{p_\| p_{0\|}}{pp_0} - \sqrt{\frac{\gamma-1}{\gamma+1}}\sqrt{\frac{\gamma_0+1}{\gamma_0-1}}\right)^2}}, \qquad (10)$$

where $p = mv/m_0c$ is a normalized relativistic momentum and indices $\|$ and $\perp$ refers to a

projection on a magnetic field.

Figure 4 displays an example distribution function (8) of a secondary electrons produced by primary electron of $\gamma_0 \approx 5$ and $\lambda_0 \equiv \frac{p_\perp^2}{p^2} = 0.2$ on the magnetic axis (color coded) and a shape of the source term approximation introduced in [3] (red curve). It can be seen that the angular distribution obtained with (8) is significantly different at the low energy region.

3. Current channel modeling

To model post-disruption plasma profiles evolution we develop a 1D transport code GTS. The cylindrical geometry is implied. Plasma of minor radius a and major radius R is surrounded by the circular resistive wall of radius b. The following set of equations is solved on the $r \in [0,a]$ domain.

Ohmic current and RE diffusion equations

$$\frac{\partial j}{\partial t} = \frac{1}{\mu_0}\frac{1}{r}\frac{\partial}{\partial r}r\frac{\partial E}{\partial r} - \frac{\partial j_{re}}{\partial t} \tag{11}$$

$$\frac{\partial j_{re}}{\partial t} = \frac{1}{r}\frac{\partial}{\partial r}D_{re}r\frac{\partial j_{re}}{\partial r} + S_{re}, \tag{12}$$

where S_{re} is a RE current source (according to [3]) and D_{re} is a radial diffusion coefficient which is an input parameter in the code.

Heat and densities diffusion

$$\frac{\partial W_{th}}{\partial t} = \frac{1}{r}\frac{\partial}{\partial r}\kappa r\frac{\partial T}{\partial r} + \frac{E^2}{\eta} + j_{re}E_c - n_e n_Z L_Z(T), \tag{13}$$

$$W_{th} = \frac{3}{2}T\left(n_e + n_H + n_Z\right) + n_H E_i^H + n_Z E_i^Z, \tag{14}$$

$$\frac{\partial n_H}{\partial t} = \frac{1}{r}\frac{\partial}{\partial r}D_H r\frac{\partial n_H}{\partial r}, \frac{\partial n_Z}{\partial t} = \frac{1}{r}\frac{\partial}{\partial r}D_Z r\frac{\partial n_Z}{\partial r}, \tag{15}$$

where κ is a heat diffusion coefficient (input parameter), η is a Spitzer resistivity, $L_Z(T)$ is a cooling coefficient according to the collisional-radiative model [11] and E_i^k is an ionization potential. The particle diffusion coefficients D_H and D_Z are input parameters.

The wall current evolution is solved together with (11)-(15)

$$\frac{\partial I_p}{\partial t} + \frac{\partial I_{wall}}{\partial t} = -\frac{I_{wall}}{\tau_{wall}}, \tag{16}$$

where τ_{wall} is a characteristic time for wall-current decay. Analytical solution for the electric field outside of $[0:a]$ domain provides and external boundary condition for (11):

$$E(a) = \frac{\mu_0}{2\pi}\frac{I_{wall}}{\tau_{wall}}ln\left(\frac{R}{b}\right) - a\left.\frac{\partial E}{\partial r}\right|_a ln\left(\frac{b}{a}\right). \tag{17}$$

For density equations (15) external fluxes can be specified

$$D_i\frac{\partial n_i(a)}{\partial r} = -P_i(t). \tag{18}$$

External boundary condition for temperature and RE are fixed values $J_{re}(a) = 0$ and $T(a) =$

T_{edge}. The code uses cubic Hermite Finite Elements with GEAR's time integration method.

For a self-consistent modeling of RE kinetic with current channel evolution the GTS code is coupled with the Monte Carlo Fokker Planck solver described in the Section 2. In this case (12) is replaced by the kinetic calculation of the $\frac{\partial j_{re}}{\partial t}$ as a function of $(\varepsilon, n_e, n_Z, E, T, B)$ for a given ensemble of test-particles which is followed through all simulation at every radial grid-point. For a faster analysis the Monte Carlo Fokker Planck solver can be used with local electric field evolution model. In this case, the plasma temperature is determined by the balance of Ohmic heating and impurity radiation and all diffusive losses are ignored.

4. Stability of plasma with runaways

The post-disruption RE current profile tends to be more peaked than the initial plasma current profile. This can be explained by non-uniformity of E/E_c profile during avalanche, RE losses to the wall, as well as the marginal stability model for the decay of RE current on a longer timescales [12]. This current profile may be MHD unstable, which would affect the RE generation and VDE dynamics, effectively limiting the timeframe for RE mitigation. To assess a possible MHD instabilities during disruptions in ITER we couple the free boundary 2D equilibrium evolution code DINA [10] with MHD stability analysis codes MISHKA [13] and CASTOR [14]. We find that both kink and tearing modes can develop during evolution of the RE current profile. These results are sensitive to post-TQ plasma profiles and RE seed current profile. Thus, predictive calculations of MHD stability of post-disruption ITER plasma would require a refined MGI gas propagation modeling as well as more reliable understanding of the TQ.

Kinetic instabilities of the RE can potentially be beneficial as a mechanism of enhanced pitch angle scattering. The candidate modes are whistlers and magnetized plasma waves. To perform the stability analysis we use a recently developed ray-tracing code COIN. The code follows a wave-packet trajectory in a realistic plasma equilibrium and integrates the runaway kinetic drive and collisional damping of the wave. It was shown, that an instability window for whistlers exists within possible ITER disruptions parameters. For runaway current of $12MA$ ($j_{re} \approx 1MA/m^2$), $n_e \approx 1.3 \cdot 10^{20} m^{-3}$ and average runaway energy of $15MeV$ (exponential spectra [3]) whistler waves may become unstable if the background plasma temperature is higher than $22eV$.

5. ITER

In ITER REs have to be mitigated by the DMS. The thermal loads during TQ and halo/eddy currents during CQ has to be mitigated as well [15]. These puts additional constraints on the RE mitigation. ITER DMS injection capabilities allow to inject up to $8kPam^3$ ($1.8 \cdot 10^{24}$ particles) of He, Ne, Ar or H2/D2 for the thermal loads mitigation and up to $100kPam^3$ ($2.2 \cdot 10^{25}$ particles) for RE mitigation. It was shown in [16] that minimal Ar density required for TQ mitigation in ITER is $\approx 10^{19} m^{-3}$.

We start calculation from a given value of RE seed current ($\approx 70kA$) after the TQ. At this point the Deuterium plasma ($n_D = 10^{20} m^{-3}$) with Argon impurity ($n_{Ar} = 10^{19} m^{-3}$) has the temperature of $9eV$ (determined by the balance between the Ohmic heating and radiative losses). The seed RE current initiates the avalanche, which reaches saturation by $\approx 15ms$. Evolution of the Ohmic current and RE current profiles during avalanche is shown in figure 5. The subsequent evolution of the RE current is shown in figure 6 for two different Argon densities created by MGI at $t = 30ms$. In the absence of MGI (red curve in figure 6) the RE current decay time

is much longer the anticipated VDE time ($\sim 500ms$). The corresponding average energy (red curve in figure 7) decays faster then the current but still too slow for successful mitigation. 2D RE distribution function at $t = 30ms$ is shown in figure 8.
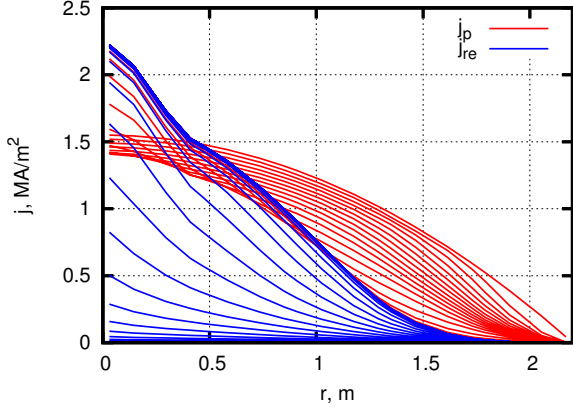

Figure 5. Red curves - consecutive plasma current profiles (decay in time); Blue curves - consecutive RE current profiles (growth in time).
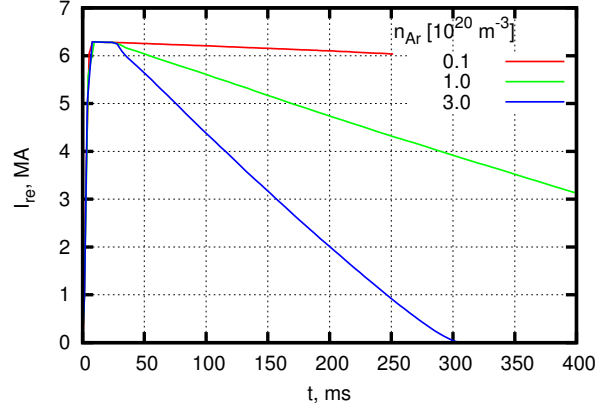

Figure 6. A mitigation of the RE current with different Ar MGI. The Ar density is introduced as a flat profile instantly at $t = 30ms$.

The green and the blue curves in figures 6 and 7 show that the decay times of the current and energy can be shortened significantly by a modest amount of Argon ($n_{Ar} = 10^{20}m^{-3}$ - green curve and $n_{Ar} = 3 \cdot 10^{20}m^{-3}$ - blue curve). These densities are within the technical limitations of the envisioned ITER MGI system. There appears to be a plateau at the average energy of around $5MeV$. The RE distribution function during this plateau phase in shown in figure 9.

The predictive calculations of RE magnetic and kinetic energy loss channels for ITER would require self-consistent studies of RE kinetics with the equilibrium evolution during the VDE. In our 1D studies the VDE

Figure 7. RE average energy evolution at different Ar density.

effects are not taken into account. In the high Argon density case (blue line in fig. 6) $I_{wall} \approx 5MA$ at $t = 300ms$ accounting for roughly half of the dissipated RE magnetic energy. The rest is dissipated by the RE collisional and radiative processes, where high-energy REs ($> 5MeV$) are affected by both radiative and collisional effects and low-energy REs are affected only by collisions.

6. Summary

In preset work we present a tool for a kinetic modeling of REs. We use a refined calculation of collisional friction force as well as full knock-on source term. The 1D version of the code allow to evaluate the effects associated with the non-uniformity of plasma profiles.

The code was used to estimate the amount of Argon that needs to be injected into RE plateau in ITER to mitigate REs on a VDE timescale.
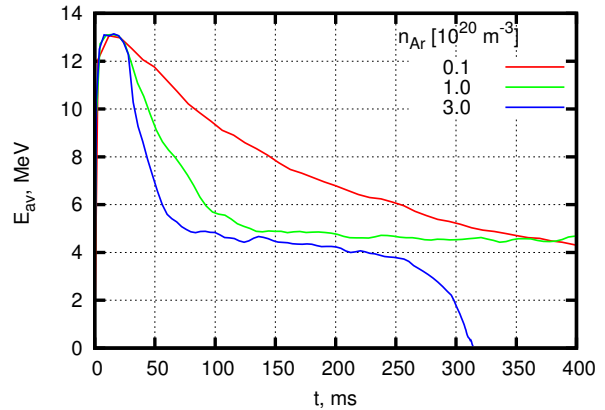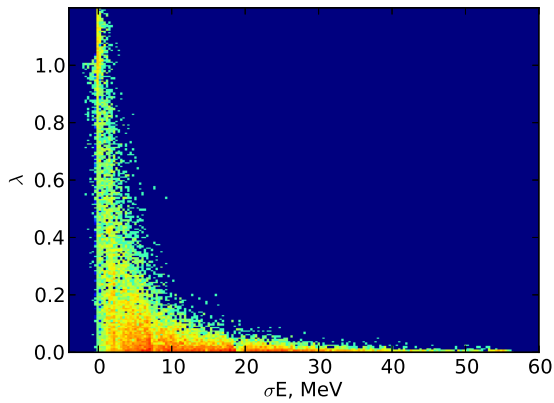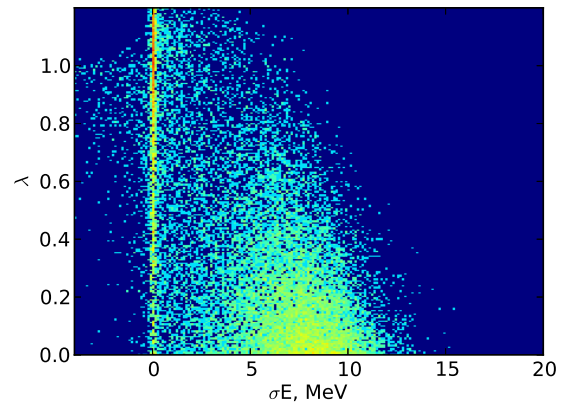
Figure 8. RE 2D distribution function at t = 30ms.

Figure 9. RE 2D distribution function at t = 100ms. $n_{Ar} = 3 \cdot 10^{20} m^{-3}$

Disclaimer: The views and opinions expressed herein do not necessarily reflect those of the ITER Organization.

References

[1] T.C. Hender et al, Progress in ITER physics basis, Chapter 3: MHD stability, operational limits and disruptions, Nucl. Fusion 47 (2007) S128-S202

[2] E. Hollmann et al, Nucl. Fusion 53 (2013) 083004 (15pp)

[3] M. Rosenbluth, S. Putvinski, Nucl. Fusion 53 (2013) 083004 (15pp)

[4] K. Aleynikova et al., 40th EPS Conference, O5.103, (2013)

[5] R. Granetz, Physics of Plasmas, 21, 072506 (2014)

[6] L.-G. Eriksson, P. Helander, Computer Physics Communications 154 (2003) 175196

[7] V.E. Zhogolev, S.V. Konovalov, "Characteristics of interaction of energetic electrons with heavy impurity ions in a tokamak plasma", to be published in VANT series Nuclear Fusion, issue 4, 2014 (in Russian)

[8] M. J. Berger, J. S. Coursey, and M. A. Zucker, ESTAR: Computer Program for Calculating Stopping-Power and Range Tables for Electrons (Version 1.2.2) (National Institute of Standards and Technology, Gaithersburg, MD, 2003), http://physics.nist.gov/Star.

[9] B. Breizman, Microinstabilities of Relativistic Runaway Electrons, 13th IAEA TM on Energetic Particles in Magnetic Confinement Systems 17 - 20 September 2013, Beijing, China

[10] R. Khayrutdinov and V. Lukash, J. Comput. Physics 109 (1993) 193-201

[11] K. B. Fournier, M. Cohen, M. J. May, and W. H. Goldstein, ATOMIC DATA AND NUCLEAR DATA TABLES 70, (1998)

[12] B. Breizman, Nucl. Fusion 54 (2014) 072002 (5pp)

[13] I. T. Chapman, S. E. Sharapov, G. T. A. Huysmans, A. B. Mikhailovskii, Physics of Plasmas 13 (6), 062511, (2006)

[14] W Kerner, JP Goedbloed, GTA Huysmans, S Poedts, E Schwarz. Journal of computational physics 142 (2), 271-303, (1998)

[15] M. Lehnen, 21st PSI Conference, Kanazawa, 2014

[16] V. Leonov et al 38th EPS Conference, 25 June 2011, Strasbourg, France